



# Z-scheme Ag-loaded g-C<sub>3</sub>N<sub>4</sub>/CuNb<sub>2</sub>O<sub>6</sub> composite photocatalyst for RhB dye degradation

Fanger Yang<sup>1</sup> · Haowen Zhang<sup>1</sup> · Qi Tang<sup>1</sup> · Shihui Lu<sup>1</sup> · Hongsheng Zhang<sup>1</sup> · Xiaohua Zheng<sup>1</sup>

Received: 24 March 2022 / Accepted: 7 August 2022 / Published online: 19 August 2022

© The Author(s), under exclusive licence to Springer Nature B.V. 2022

## Abstract

Photocatalysis is considered to be one of the possible routes to solve energy crises at a low cost. Graphitic-C<sub>3</sub>N<sub>4</sub> combined with other semiconductors at the nanoscale has demonstrated a promising potential in photocatalysis application owing to the heterojunction configuration. In this study, Ag/g-C<sub>3</sub>N<sub>4</sub>/CuNb<sub>2</sub>O<sub>6</sub>-4 (mass ratio of CuNb<sub>2</sub>O<sub>6</sub> to g-C<sub>3</sub>N<sub>4</sub> = 1:4) composites were prepared by photo-deposition of Ag particles on the hydrothermally synthesized g-C<sub>3</sub>N<sub>4</sub>/CuNb<sub>2</sub>O<sub>6</sub>-4 composites. The microstructure, morphology, and light absorption property of the photocatalysts were characterized by X-ray diffractometry, scanning electron microscopy, transmission electron microscopy, X-ray photoelectron spectroscopy, and UV–Vis diffuse reflectance spectroscopy. The photocatalytic properties of photocatalysts and active species responsible for the degradation of RhB dye under visible light were investigated. After loading Ag particles on the g-C<sub>3</sub>N<sub>4</sub>/CuNb<sub>2</sub>O<sub>6</sub>-4 composites, the resulting Ag/g-C<sub>3</sub>N<sub>4</sub>/CuNb<sub>2</sub>O<sub>6</sub>-4 composites show a bandgap of ~2.31 eV and a significant increase in photocatalytic efficiency. In particular, the photocatalytic activity of 11% Ag/g-C<sub>3</sub>N<sub>4</sub>/CuNb<sub>2</sub>O<sub>6</sub>-4 composite (Ag mass fraction = 11%) is nearly seven times that of orthorhombic CuNb<sub>2</sub>O<sub>6</sub> and 3.8 times that of g-C<sub>3</sub>N<sub>4</sub>/CNO-4 composite. The Z-scheme heterojunction has been successfully formed in the Ag/g-C<sub>3</sub>N<sub>4</sub>/CuNb<sub>2</sub>O<sub>6</sub>-4 composites and it enhances the photocatalytic performance significantly with the best degradation efficiency of 88% after 2 h.

**Keywords** g-C<sub>3</sub>N<sub>4</sub>/CuNb<sub>2</sub>O<sub>6</sub> · Photocatalytic degradation · Z-scheme heterojunction · Hydrothermal method · Rhodamine b

✉ Xiaohua Zheng  
zhengxh@zjut.edu.cn

<sup>1</sup> College of Materials Science and Engineering, Zhejiang University of Technology, Hangzhou 310014, People's Republic of China

## Introduction

In recent decades, environmental and energy crises have become more severe than ever before [1, 2]. The widespread use of synthetic dyes has resulted in large amounts of wastewater [3–5] containing various synthetic dyes [6, 7], such as azo, anthraquinone, sulfur, indigo and triphenylmethyl. Amidst the rising cost of pollutant disposal [8], utilizing solar energy via photocatalysts is unambiguously an effective strategy to solve the crises [9]. The photocatalysis technique not only converts sunlight into a valuable source of energy [10] but also directly uses sustainable solar energy to solve the environmental crises.

Photocatalytic degradation is an effective advanced oxidation process (AOP) to dispose of a small amount of industrial wastewater. AOP is based on hydroxyl radical, an active oxidant that can rapidly and non-selectively oxidize many organic contaminants [11–13]. The photocatalytic reaction requires absorption of photons of sufficient energy and a favorable redox potential of the photocatalytic semiconductors [14, 15] because the common photocatalysts are activated only by ultraviolet light. Herein, the use of photocatalysts with better photocatalytic performance and higher efficiency under visible light may have broader prospects.

Niobate is a widely used ferroelectric, piezoelectric, and luminescent material owing to its unique crystal structure and physicochemical properties. In catalytic reactions, niobates show extraordinary catalytic activity and stability under acidic conditions [16]. Niobate photocatalysts were usually prepared using solution combustion synthesis, liquid-phase synthesis, and solid-state reaction [17–19]. A low-cost and environmentally friendly photocatalyst,  $\text{CuNb}_2\text{O}_6$  shows a favorable band gap of 1.90 eV [20] and can also provide a superior light absorption region after combining with other semiconductors [21]. However, due to the fast recombination of photogenerated carriers in  $\text{CuNb}_2\text{O}_6$ , the photocatalytic performance of  $\text{CuNb}_2\text{O}_6$  needs to be improved further.

$\text{g-C}_3\text{N}_4$  is another attractive photocatalyst owing to its favorable bandgap (2.70 eV) [22]. With a two-dimensional structure,  $\text{g-C}_3\text{N}_4$  was reported to have an excellent photocatalytic performance [23–25]. The photocatalytic activity of  $\text{g-C}_3\text{N}_4$  is still limited by the high recombination rate of photogenerated carriers and the low specific surface area of the catalyst [26]. Qi et al. found that by loading Ag on  $\text{g-C}_3\text{N}_4$  nanosheets, the photocatalytic activity of the porous  $\text{g-C}_3\text{N}_4$  nanosheets improved effectively [27]. In addition, the study [28] also showed that the  $\text{g-C}_3\text{N}_4/\text{CuNb}_2\text{O}_6$  composites could effectively enhance the absorption of UV–visible light in photocatalysis, but due to their low carrier separation efficiency and weak REDOX capacity the photocatalytic activity becomes limited.

In this study, we report a heterojunction to improve the photocatalytic activity of the  $\text{g-C}_3\text{N}_4$ -based catalyst by recombining three phases:  $\text{CuNb}_2\text{O}_6$ ,  $\text{g-C}_3\text{N}_4$ , and Ag. The orthorhombic  $\text{CuNb}_2\text{O}_6$  phase and  $\text{g-C}_3\text{N}_4/\text{CuNb}_2\text{O}_6$  composites were synthesized using the hydrothermal method. A series of  $\text{Ag/g-C}_3\text{N}_4/\text{CuNb}_2\text{O}_6$  composites with different mass fractions of Ag was prepared by the photo-deposition of Ag on the surface of  $\text{g-C}_3\text{N}_4/\text{CuNb}_2\text{O}_6$  composites. The microstructure and photocatalytic properties of the composites responsible for degradation of

RhB dye were investigated. The effect of mass fractions of Ag on photocatalytic activity of the composites and the synergistic photocatalytic mechanism was discussed further. The addition of Ag was expected to effectively improve the carrier mobility, separation efficiency of photogenerated electron–hole pairs and promote the formation of an all-solid Z-scheme heterojunction. This further helped to achieve a significantly higher photocatalytic activity under the conditions of low catalyst concentration and lesser light power.

## Preparation of g-C<sub>3</sub>N<sub>4</sub>-based photocatalysts

The g-C<sub>3</sub>N<sub>4</sub>, Nb<sub>2</sub>O<sub>5</sub>, RhB, and AgNO<sub>3</sub> were purchased from Shanghai Aladdin Biochemical Technology Co., LTD. Citric acid, cupric acetate, and ammonia were purchased from China National Pharmaceutical Group Corporation. All chemical reagents were of analytical grade and used without further purification.

### Synthesis of orthorhombic CuNb<sub>2</sub>O<sub>6</sub>

The orthorhombic CuNb<sub>2</sub>O<sub>6</sub> phase was synthesized by hydrothermal method using a precursor. The specific steps involved in the synthesis are shown in Fig. 1. In order to prepare the precursor, Nb<sub>2</sub>O<sub>5</sub> was dissolved in hydrofluoric acid at 130 °C for 6 h. Furthermore, all Nb<sup>5+</sup> ions were composited into the sediment prepared by adding ammonia dropwise to the solution, and subsequently, Nb-containing powder was obtained by drying the sediment. In addition, the Nb-containing powder, citric acid, and cupric acetate with a molar ratio  $n(\text{Nb}^{5+}) : n(\text{citric acid}) : n(\text{Cu}^{2+})$  of 1:3:1 were added to deionized water, and the suspension was continuously stirred until all the mixture dissolved. Finally, the solution mixture was heated in a water bath at 80 °C until a blue colloidal solution was obtained, which was the precursor. After

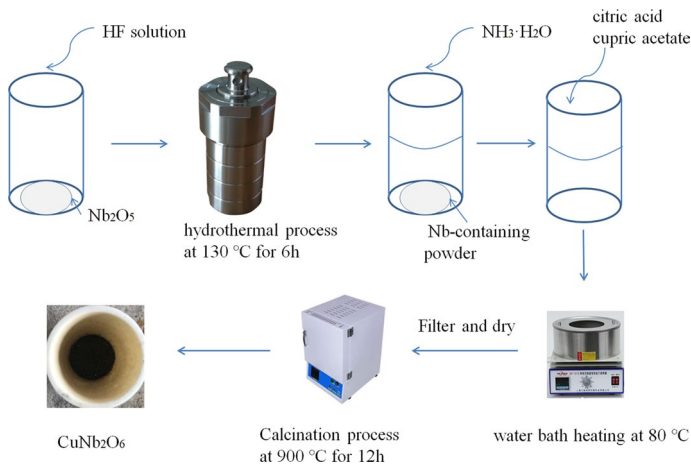


**Fig. 1** Synthetic route for preparation of o-CNO phase

calcining the precursor at 900 °C for 12 h, the orthorhombic  $\text{CuNb}_2\text{O}_6$  (labeled as o-CNO) powder was obtained.

### Preparation of Ag/g- $\text{C}_3\text{N}_4$ /CNO composites

The g- $\text{C}_3\text{N}_4$ /CNO-4 composite (mass ratio of CNO: g- $\text{C}_3\text{N}_4$  is 1:4) was hydrothermally synthesized at 130 °C for 12 h. Prior to the synthesis, the salts with a required mass ratio were mixed and stirred in the beaker for 30 min to produce a suspension. This suspension was ultrasonically dispersed for 10 min to ensure the good dispersion of salts. The Ag/g- $\text{C}_3\text{N}_4$ /CNO-4 composites were prepared by the photo-deposition method. The g- $\text{C}_3\text{N}_4$ /CNO-4 composite with a fixed mass of 100 mg was dispersed in deionized water and the solution mixture was continuously stirred using a magnetic stirrer. Then the desired volume of  $\text{AgNO}_3$  solution (1 mmol/L), corresponding to  $\text{AgNO}_3$  mass of 1.58, 7.87, 17.32, 26.77, and 47.24 mg, respectively, was added to the suspension in dark and stirred for 1 h. Subsequently, the suspension was irradiated with a Xe lamp for 30 min with continuous stirring. The final sample was obtained by removing the water via filtration followed by drying at 60 °C for 12 h. The complete decomposition of  $\text{AgNO}_3$  was confirmed by the detection of Ag cation content. The obtained composites were labeled as 1% Ag/g- $\text{C}_3\text{N}_4$ /CNO-4, 5% Ag/g- $\text{C}_3\text{N}_4$ /CNO-4, 11% Ag/g- $\text{C}_3\text{N}_4$ /CNO-4, 17% Ag/g- $\text{C}_3\text{N}_4$ /CNO-4, and 30% Ag/g- $\text{C}_3\text{N}_4$ /CNO-4 in terms of Ag content.

### Characterization

The crystal structure of the composites was characterized by an X-ray diffractometer (XRD, Thermo X'TRA). The X-ray diffraction (XRD) patterns were recorded with a  $\text{Cu K}\alpha$  radiation operating at a tube voltage of 40 kV, tube current of 40 mA, scanning speed of 2°/min, and  $2\theta$  range of 10°–80°. The surface morphology and elemental distribution of the synthesized CNO and Ag/g- $\text{C}_3\text{N}_4$ /CNO composites were observed by scanning electron microscope (SEM, Hitachi-S4700) and built-in energy-dispersive spectrometer (EDS). The fine microstructure of the composites was observed by a high-resolution transmission electron microscope (HRTEM, Tecnai G2 F30 S-Twin) with an accelerating voltage of 300 kV. X-ray photoelectron spectroscopy (XPS, Kratos AXIS Ultra DLD) was performed with a monochromatic Al  $\text{K}\alpha$  ray (1486.7 eV) and pass energy of 20 eV. The Shirley baseline subtraction was used in the fitting. The light absorption property and band gap of the composites were determined by an American PE Lambda A750 UV–visible (UV/Vis) near-infrared spectrophotometer equipped with an integrating sphere attachment. The migration, transfer, and recombination of photogenerated electron–hole pairs were characterized by fluorescence spectrophotometer (Hitachi F-4600) at an excitation wavelength of 245 nm. The specific surface areas of the composites were determined by Brunauer–Emmett–Teller (BET) surface area test (ASAP 2010) based on nitrogen gas adsorption and desorption. The electrochemical tests were performed by a CHI660E electrochemical workstation with a three-electrode cell. The potential values were relative to the Ag/AgCl electrode. The active free radicals involved

in the photocatalytic process were characterized by electron spin resonance spectroscopy (ESR, Bruker E500). 5,5-dimethyl-1-pyrroline N-oxide (DMPO) was used as the trapping agent. The assays of hydroxyl radical ( $\cdot\text{OH}$ ) and superoxide radical ( $\cdot\text{O}_2^-$ ) were conducted after irradiating the catalyst for 5 min in H<sub>2</sub>O and CH<sub>3</sub>OH, respectively. The holes generated during the photocatalytic process were tested directly with the catalyst.

### Photocatalytic reaction

Rhodamine B (RhB) dye was chosen as the model pollutant and photocatalytic activity of the composites was tested through degradation of RhB solution under a 200-W Xe lamp in open air and at room temperature. The catalyst with a mass of 10 mg was added to the RhB solution (10 mg/L, 50 mL) in a beaker. Prior to irradiation, the solution was stirred on the magnetic stirrer for 30 min in dark to achieve the adsorption–desorption equilibrium. The absorbance of RhB solution was measured by ultraviolet spectrophotometer at 554 nm where the strongest peak of RhB was seen and the concentration of RhB in solution was calculated from a working curve. The degradation efficiency was calculated according to formula (1):

$$\eta\% = \frac{c_0 - c}{c_0} \times 100\% \quad (1)$$

where  $c_0$  is the original concentration of RhB and  $c$  is the RhB concentration after degradation.

In addition, cyclic experiments were carried out four times to test the stability of the catalysts. The catalysts were separated by centrifuge (TD5A) and ultrasonically rinsed in deionized water for 3 times at the end of each experiment. A similar cyclic photocatalytic activity was obtained with the method described above.

### Active species trapping experiment

Oxalic acid, 2-propanol (IPA), and 1,4-benzoquinone (BQ) were used as trapping agents for hole ( $\text{h}^+$ ), hydroxyl radical ( $\cdot\text{OH}$ ), and superoxide radical ( $\cdot\text{O}_2^-$ ), respectively. The active species trapping experiments were similar to that of the photocatalytic experiments except for the addition of 1 mmol of trapping agent. The inhibitory effects of the active species were characterized by the degradation efficiency of RhB in visible light irradiation system under a Xe lamp in open air and at room temperature.

## Results and discussion

### Microstructure of photocatalysts

XRD patterns of the samples are shown in Fig. 2. The diffraction peaks for o-CNO obtained at 24.7°, 30.3°, and 35.0° could be assigned to the (310), (311), and (002)

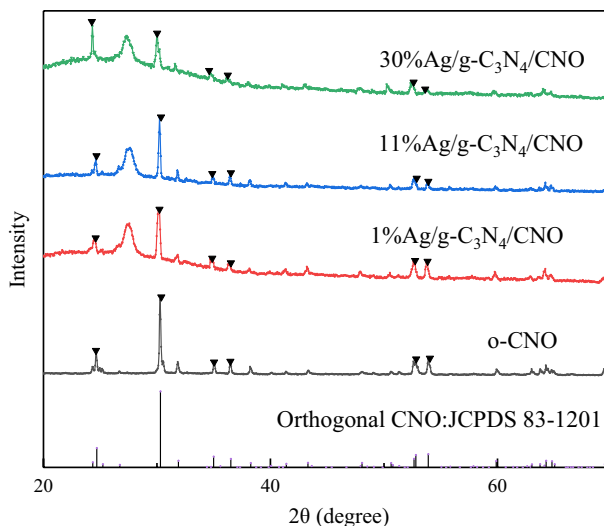


**Fig. 2** XRD patterns for o-CNO and Ag/g-C<sub>3</sub>N<sub>4</sub>/CNO-4 samples

reflections of orthorhombic CuNb<sub>2</sub>O<sub>6</sub> (JCPDS 83-1201, space group Pbcn), respectively, suggesting that the sample had orthorhombic structure and high purity. The peaks for Ag/g-C<sub>3</sub>N<sub>4</sub>/CNO-4 composites at 27.5° could be assigned to the (110) reflection of g-C<sub>3</sub>N<sub>4</sub>, indicating that the graphite-like lamellar structure of the g-C<sub>3</sub>N<sub>4</sub> phase was intact. Moreover, none of the Ag/g-C<sub>3</sub>N<sub>4</sub>/CNO-4 samples showed diffraction peaks from the Ag phase because of the nanocrystalline structure and high dilution effect of the Ag phase [28, 29].

Figure 3 shows SEM morphologies of the samples. As shown in Fig. 3a, the o-CNO sample was granular, and the particle diameter ranged from 0.2 to 0.6 μm.

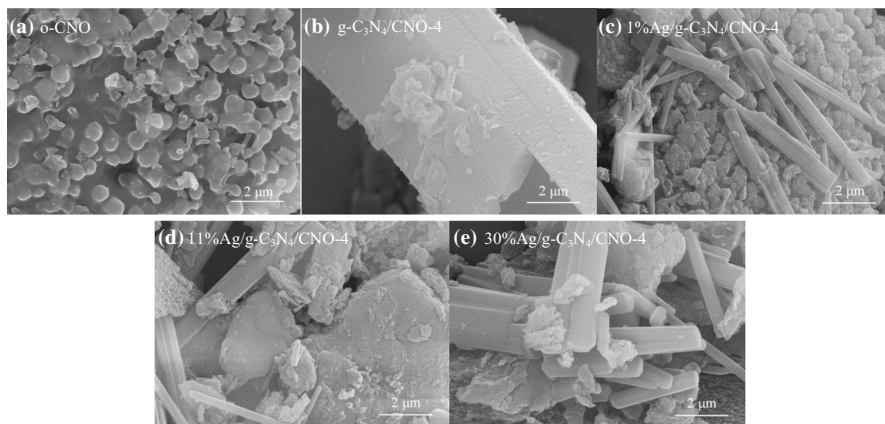


**Fig. 3** SEM morphology of the samples

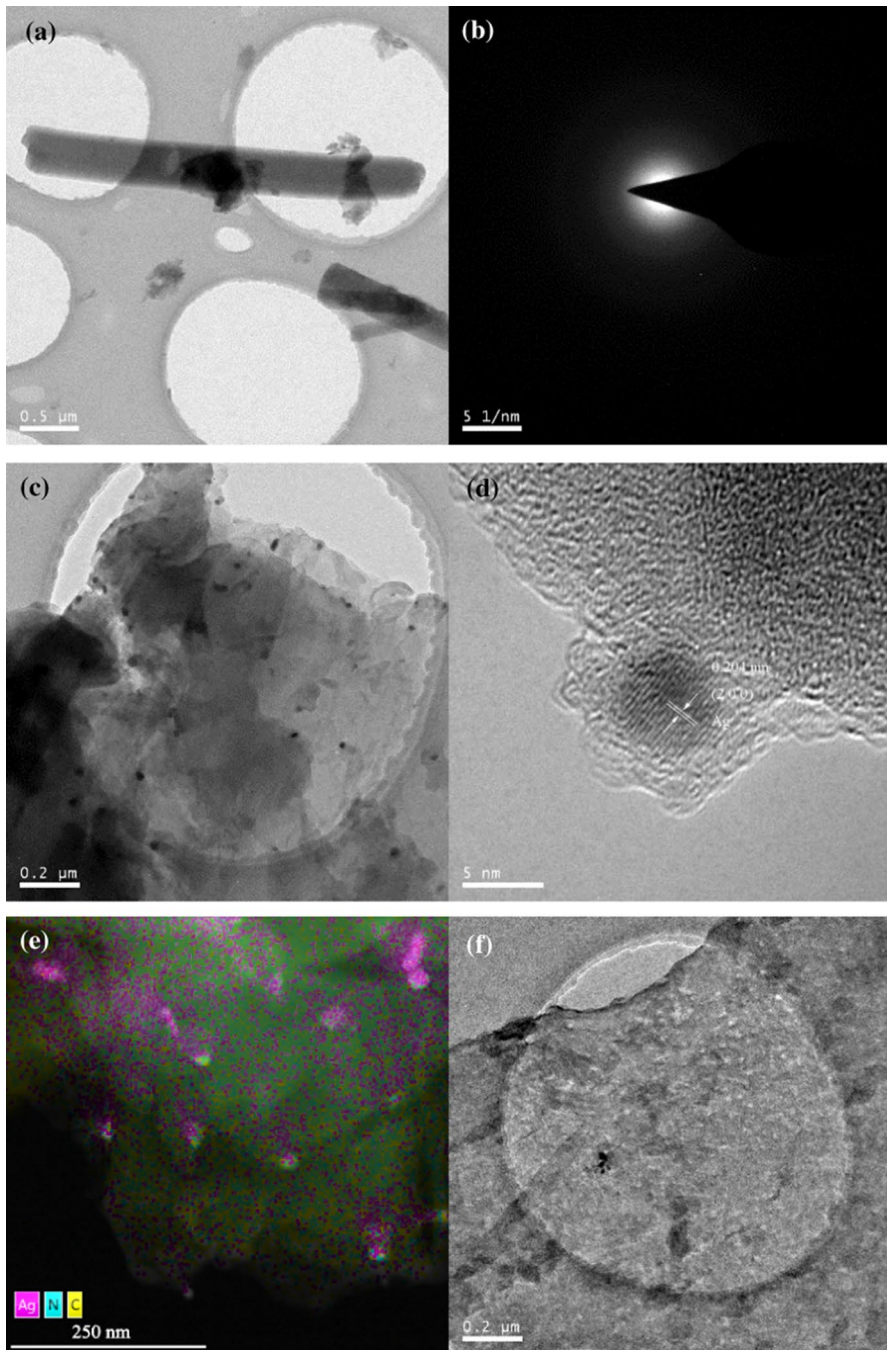
Usually, the porous structure can increase the specific surface area of powders and facilitate the formation of heterojunction with other phases. In Fig. 3b, the C<sub>3</sub>N<sub>4</sub> phase in the g-C<sub>3</sub>N<sub>4</sub>/CNO-4 composite consisted of clustered g-C<sub>3</sub>N<sub>4</sub> rods, and the CNO particles were coated on the surface of the C<sub>3</sub>N<sub>4</sub> phase to form a heterojunction. As shown in Fig. 3c–e, the rod-like C<sub>3</sub>N<sub>4</sub> was well-coated on the surface of granular copper niobate to form a composite with nanoscale Ag particles distributed throughout the surface.

Figure 4 shows TEM images of 11% Ag/g-C<sub>3</sub>N<sub>4</sub>/CNO-4 composite. The obvious rod-like structures of the g-C<sub>3</sub>N<sub>4</sub> phase as shown in Fig. 4a and the corresponding electron diffraction pattern (Fig. 4b) suggests an amorphous structure for the g-C<sub>3</sub>N<sub>4</sub> phase. As shown in Fig. 4c, the Ag particles (see the lattice lines of metallic Ag in Fig. 4d) with a diameter smaller than 20 nm were uniformly dispersed on the amorphous g-C<sub>3</sub>N<sub>4</sub> components. The EDS element mapping (Fig. 4e) further confirmed the distribution of Ag nanoparticles. The TEM image of the g-C<sub>3</sub>N<sub>4</sub>/CNO-4 heterojunction (Fig. 4f) and corresponding high-resolution image (Fig. 4g) demonstrated a crystalline CNO phase (the electron diffraction pattern as shown in Fig. 4h) above the dashed line and an amorphous g-C<sub>3</sub>N<sub>4</sub> phase below the dashed line in the heterojunction.

In addition, according to the adsorption–desorption curves in BET tests (Fig. 5), the specific surface area of g-C<sub>3</sub>N<sub>4</sub>, o-CNO, g-C<sub>3</sub>N<sub>4</sub>/CNO-4, and 11% Ag/g-C<sub>3</sub>N<sub>4</sub>/CNO-4 sample was 22.7, 2.74, 39.2, and 38.4 m<sup>2</sup>/g, respectively. This further suggests that the heterojunction had a large specific surface area which increased after the two phases recombined. However, no significant change in the specific surface area was seen after the addition of silver. Therefore, the deposition of silver on the g-C<sub>3</sub>N<sub>4</sub>/CNO-4 heterojunction was not conducive to improve the specific surface area of the photocatalysts.

Figure 6 shows the X-ray photoelectron spectrum of pure g-C<sub>3</sub>N<sub>4</sub>, o-CNO and 11% Ag/g-C<sub>3</sub>N<sub>4</sub>/CNO-4 nanocomposite. The charging effect of the samples was corrected by referring to C1s 284.6 eV. The fitting results related to the position of peaks are shown in Table 1. In the Ag3d spectrum, the binding energy centered at 368.1 and 374.1 eV corresponds to metallic Ag (3d<sub>5/2</sub>) and Ag (3d<sub>3/2</sub>), respectively, which suggests the presence of metallic Ag in 11% Ag/g-C<sub>3</sub>N<sub>4</sub>/CNO-4 catalyst [30, 31]. In the C1s spectrum, the peak located at 284.6 eV was assigned to the sp<sup>2</sup> C–C bond in g-C<sub>3</sub>N<sub>4</sub>, and the peaks at 287.9 and 288.0 eV were assigned to the N–C=N groups in g-C<sub>3</sub>N<sub>4</sub> for 11% Ag/g-C<sub>3</sub>N<sub>4</sub>/CNO-4 nanocomposite and pure g-C<sub>3</sub>N<sub>4</sub>, respectively [30]. For the N1s spectrum, the two peaks centered at 398.5 and 400.2 eV for 11% Ag/g-C<sub>3</sub>N<sub>4</sub>/CNO-4 nanocomposite, and the peaks at 398.5 and 400.0 eV for pure g-C<sub>3</sub>N<sub>4</sub>, correspond to the C=N–C and N–(C)<sub>3</sub> groups, respectively [32]. The results from N1s and C1s spectrum clearly proved the existence of g-C<sub>3</sub>N<sub>4</sub> in the catalysts. In the Cu2p spectrum, the peaks centered at 934.0 and 953.9 eV for 11% Ag/g-C<sub>3</sub>N<sub>4</sub>/CNO-4 nanocomposite were attributed to Cu (2p<sub>3/2</sub>) and Cu (2p<sub>1/2</sub>) from Cu–O bonds with a 19.9 eV splitting spacing of 2p doublet [33, 34], whereas the additional peaks at 941.9 and 961.9 eV correspond to the shake-up satellites from Cu–O bonds in the catalysts [35]. For pure o-CNO, the peaks for Cu (2p<sub>3/2</sub>) and Cu (2p<sub>1/2</sub>) were located at 934.3 and 954.4 eV, respectively, with a splitting spacing of 20.1 eV, which caused a slight shift compared to those of 11%





**Fig. 4** HRTEM images of the as-synthesized 11% Ag/g-C<sub>3</sub>N<sub>4</sub>/CNO-4 photocatalyst



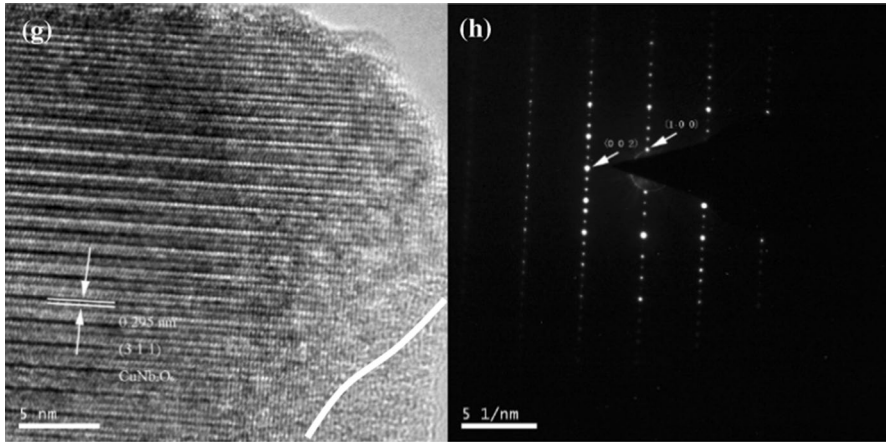


**Fig. 4** (continued)

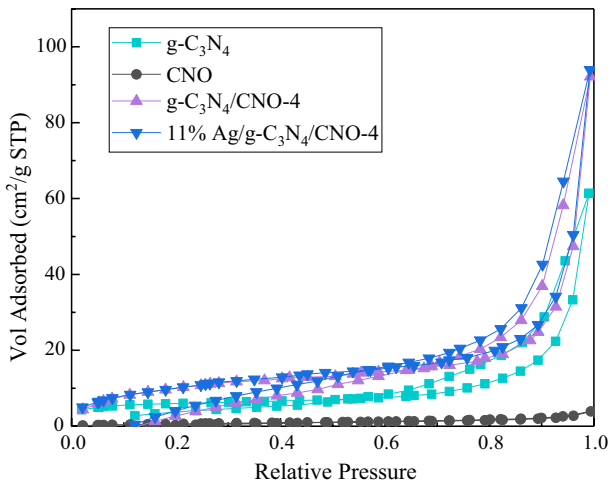


**Fig. 5** Nitrogen gas adsorption–desorption curves of the as-synthesized photocatalysts

Ag/g-C<sub>3</sub>N<sub>4</sub>/CNO-4 nanocomposite. The Nb3d spectrum of 11% Ag/g-C<sub>3</sub>N<sub>4</sub>/CNO-4 nanocomposite showed the two main peaks, Nb (3d<sub>3/2</sub>) and Nb (3d<sub>5/2</sub>), located at 209.6 and 206.9 eV, respectively. The splitting energy between Nb (3d<sub>3/2</sub>) and Nb (3d<sub>5/2</sub>) was 2.7 eV. According to previous reports, this splitting energy was 2.72 eV in LiNbO<sub>3</sub> [36] and 2.70 eV in CaNb<sub>2</sub>O<sub>6</sub> [37]. For pure o-CNO, the two peaks were located at 209.7 and 207.0 eV, and the splitting spacing of the doublet was the same as that of the 11% Ag/g-C<sub>3</sub>N<sub>4</sub>/CNO-4 nanocomposite. For 11% Ag/g-C<sub>3</sub>N<sub>4</sub>/CNO-4 nanocomposite, the O1s spectrum was deconvoluted into three peaks located at 530.1, 531.7, and 532.9 eV, which could be successively attributed to the Nb–O and Cu–O bonds in o-CNO, and H–O bonds from water vapor adsorbed on the surface

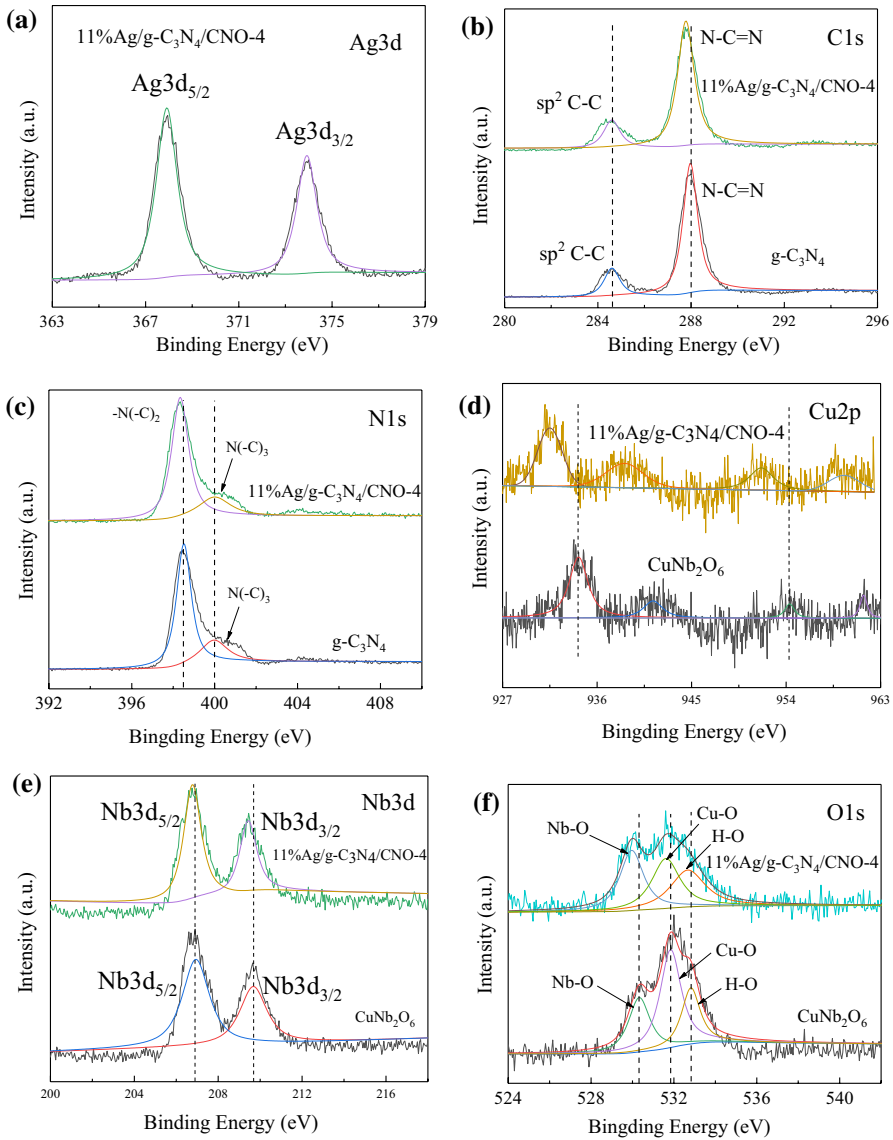


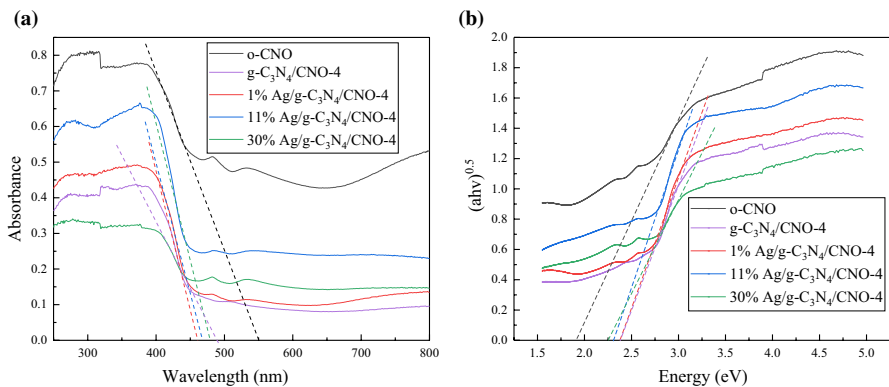
**Fig. 6** High-resolution XPS spectra of the **a** Ag3d, **b** C1s, **c** N1s, **d** Cu2p, **e** Nb3d, and **f** O1s for pure g-C<sub>3</sub>N<sub>4</sub>, o-CNO, and 11% Ag/g-C<sub>3</sub>N<sub>4</sub>/CNO composite

[38]. However, these peaks caused a slight shift compared to those of pure o-CNO. Based on the above results, a certain chemical shift was observed in the binding energy of bonds in 11% Ag/g-C<sub>3</sub>N<sub>4</sub>/CNO-4 nanocomposite, which further suggests that a chemical interaction was involved.

Figure 7a shows the UV/Vis spectra of o-CNO and Ag/g-C<sub>3</sub>N<sub>4</sub>/CNO-4 composites. It was seen that o-CNO mainly absorbed light of wavelength below 550 nm

**Table 1** Fitting results of XPS for g-C<sub>3</sub>N<sub>4</sub>, o-CNO, and 11% Ag/g-C<sub>3</sub>N<sub>4</sub>/CNO-4

Spectrum	Peak	Binding energy (eV)		
		g-C <sub>3</sub> N <sub>4</sub>	o-CNO	11%Ag/g-C <sub>3</sub> N <sub>4</sub> /CNO-4
Ag3d	Ag3d <sub>5/2</sub>	—	—	368.1
	Ag3d <sub>3/2</sub>	—	—	374.1
C1s	sp <sup>2</sup> C–C	284.6	—	284.6
	N–C=N	288.0	—	287.9
N1s	C=N–C	398.5	—	398.5
	N-(C) <sub>3</sub>	400.0	—	400.2
Cu2p	Cu2p <sub>3/2</sub>	—	934.4	934.0
	Cu2p <sub>1/2</sub>	—	954.5	953.9
Nb3d	Nb3d <sub>5/2</sub>	—	207.0	206.9
	Nb3d <sub>3/2</sub>	—	209.7	209.6
O1s	Nb–O	—	530.3	530.1
	Cu–O	—	531.8	531.7
	H–O	—	532.8	532.9

**Fig. 7** **a** UV/Vis diffuse reflection spectra and **b** Tauc plots of the as-synthesized photocatalysts

and the g-C<sub>3</sub>N<sub>4</sub>/CNO-4 composite exhibited a lower light absorption intensity than o-CNO. The light absorption intensities of Ag/g-C<sub>3</sub>N<sub>4</sub>/CNO-4 composites with Ag content of 1% and 11% were higher than that of g-C<sub>3</sub>N<sub>4</sub>/CNO-4 due to the loading of Ag, and their absorption edge wavelengths were ~470 nm. The 11% Ag/g-C<sub>3</sub>N<sub>4</sub>/CNO-4 composite exhibited the highest absorption intensity among these composites, which further suggests that the 11% Ag/g-C<sub>3</sub>N<sub>4</sub>/CNO-4 composite had a better utilization rate of visible light. The reasonable explanation was that, after loading Ag, the more refined grains of g-C<sub>3</sub>N<sub>4</sub> and o-CNO and the close interaction between g-C<sub>3</sub>N<sub>4</sub> and o-CNO increased the light scattering, thereby increasing the transmission length of incident light and enhancing the visible light capturing ability

of g-C<sub>3</sub>N<sub>4</sub>/CNO composites. Due to the excessive metallic Ag on its surface, the composite 30% Ag/g-C<sub>3</sub>N<sub>4</sub>/CNO-4 demonstrated a relatively low light absorption intensity.

In addition, the Kubelka–Munk formula (2) was used to calculate the band gap energy of the photocatalysts:

$$\alpha h\nu = A(h\nu - E_g)^{\frac{n}{2}} \quad (2)$$

In formula (2),  $\alpha$ ,  $h$ ,  $\nu$ ,  $A$ , and  $E_g$  are the absorption coefficient, Planck constant, optical frequency, constant, and band gap, respectively. The value of  $n$  was determined by the band gap type of semiconductors and for an indirect transition semiconductor,  $n$  equals 4. Figure 7b shows the curves of  $(\alpha h\nu)^{0.5}$  on  $h\nu$  for o-CNO and Ag/g-C<sub>3</sub>N<sub>4</sub>/CNO composites. Consequently, the band gap of o-CNO was 1.90 eV, similar to the previous reports [20], and the band gaps of g-C<sub>3</sub>N<sub>4</sub>/CNO-4 and Ag/g-C<sub>3</sub>N<sub>4</sub>/CNO-4 composites were ~2.31 eV.

Figure 8 shows the PL spectra of o-CNO and Ag/g-C<sub>3</sub>N<sub>4</sub>/CNO-4 composites. In general, the photoluminescence emission is generated by the recombination of photoelectron–hole pairs. The higher the recombination rate of electron–hole pairs, the higher is the fluorescence intensity, and the lower is the photocatalytic performance. Recent research studies showed that the PL spectrum of g-C<sub>3</sub>N<sub>4</sub> demonstrated a relatively wide and strong fluorescence emission peak at 450 nm [39, 40]. The peak around 450 nm which occurs in the PL spectrum of Ag/g-C<sub>3</sub>N<sub>4</sub>/CNO-4 composites was majorly because of the presence of g-C<sub>3</sub>N<sub>4</sub> component in the composites. However, it was observed that Ag-loading reduced the photoluminescence emission effect and thus the photoluminescence intensity was negatively correlated with Ag content. After the formation of the composite, the absorption peak showed a slight blue shift, which might be attributed to the enhanced absorption ability of

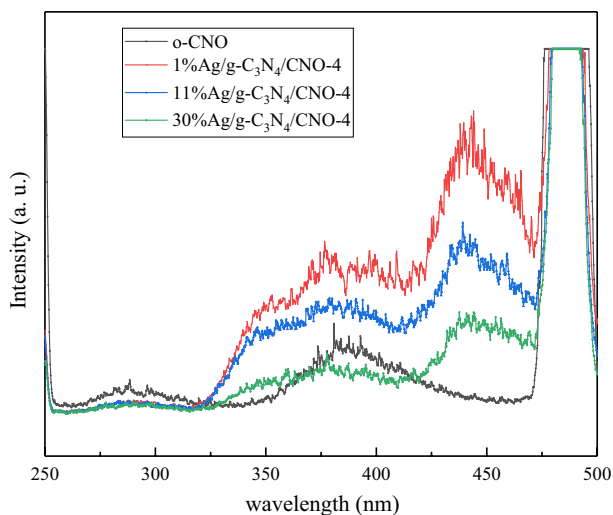


**Fig. 8** Fluorescence emission spectra of o-CNO and Ag/g-C<sub>3</sub>N<sub>4</sub>/CNO-4 with different Ag contents

the composite to UV–visible light. These results indicate that Ag-loading effectively inhibited the recombination of photoelectron–hole pairs in g-C<sub>3</sub>N<sub>4</sub>/CNO composite catalyst, which was conducive to the separation of photocarriers, thus improving the photocatalytic activity of the composite.

### Analysis of photocatalytic activity of g-C<sub>3</sub>N<sub>4</sub>-based heterostructured composites

The photodegradation efficiency directly expressed the photocatalytic performance of materials as one of the important indexes of composite photocatalysts. Figure 9 shows the photocatalytic activity of the Ag/g-C<sub>3</sub>N<sub>4</sub>/CNO-4 composite with different Ag contents for degradation of RhB. The degradation efficiency of o-CNO and g-C<sub>3</sub>N<sub>4</sub>/CNO-4 was found to be 11.47% and 27.7%, respectively, and each of the Ag/g-C<sub>3</sub>N<sub>4</sub>/CNO-4 composites exhibited a higher degradation efficiency than the above two, which further suggests that the heterojunction was successfully fabricated. It was noteworthy that 11%Ag/g-C<sub>3</sub>N<sub>4</sub>/CNO-4 composite showed the highest degradation efficiency of 82.07%, which was about 7.1 times that of o-CNO and 3.8 times that of g-C<sub>3</sub>N<sub>4</sub>/CNO-4, and as a result showed the best photocatalytic performance. However, the decrease in degradation efficiency with an excessive Ag-loading content for the samples might be attributed to the reduction in light reflection and to the amount of active sites present on the composite surface owing to the shadowing effect of Ag particles. As a result, the 30% Ag/g-C<sub>3</sub>N<sub>4</sub>/CNO-4 sample showed reduced fluorescence intensity in PL test whereas o-CNO showed low photocatalytic efficiency but better light absorption in the UV/Vis experiment.

According to the Langmuir–Hinshelwood model, the rate constant ( $k$ ) during the degradation process was used to characterize the change of dye concentration with irradiation time by measuring the change in absorbance of RhB. As shown in Fig. 10, the rate constant of 11% Ag/g-C<sub>3</sub>N<sub>4</sub>/CNO-4 composite showed the highest

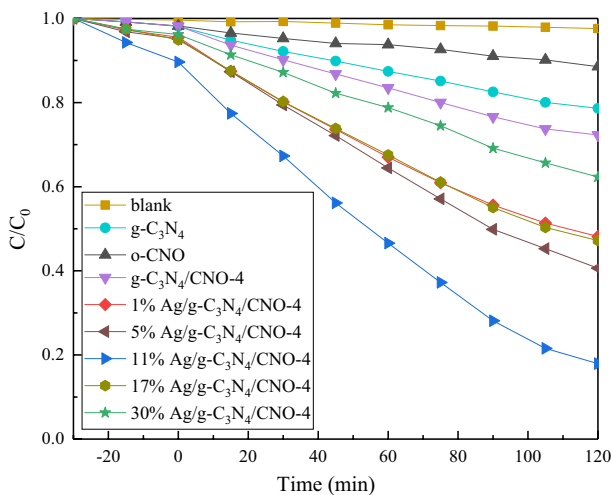
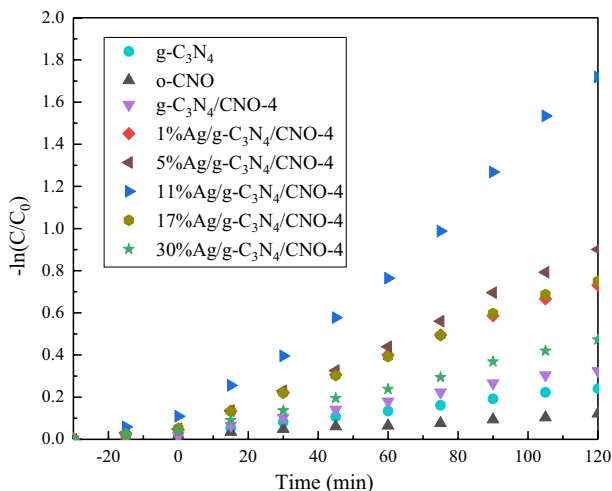


Fig. 9 Photocatalytic diagrams of Ag/g-C<sub>3</sub>N<sub>4</sub>/CNO-4 composites with different Ag contents



**Fig. 10** Kinetic simulation of the degradation of RhB by Ag/g-C<sub>3</sub>N<sub>4</sub>/CNO-4 composites

value of  $0.859 \text{ h}^{-1}$ , and the degradation rate gradually decreased with increasing test time. The results imply that the degradation rate of RhB decreases with a decrease in RhB concentration.

The stability of photocatalyst is an important property. Figure 11a shows the XRD patterns of the 11% Ag/g-C<sub>3</sub>N<sub>4</sub>/CNO-4 photocatalyst before and after cyclic experiments. On comparing with the pattern before cyclic experiments it was found that the phase structure in the catalysts hardly changed after cyclic experiments. Meanwhile, the photocatalytic degradation efficiency showed a slight decrease with the number of cycles (Fig. 11b), which clearly suggests that the prepared catalysts have good stability.

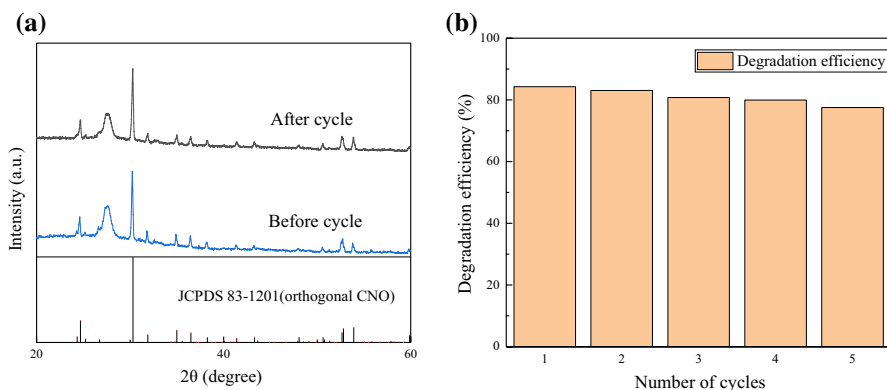


**Fig. 11** **a** XRD patterns of 11% Ag/g-C<sub>3</sub>N<sub>4</sub>/CNO-4 composite before and after cyclic experiments and **b** dependence of degradation efficiency with number of cycles of the photocatalyst



According to the data from research studies, the comparison of photocatalytic performance of g-C<sub>3</sub>N<sub>4</sub>-based and CuNb<sub>2</sub>O<sub>6</sub>-based materials for degradation of various dyes is shown in Table 2. The Ag/g-C<sub>3</sub>N<sub>4</sub>/CuNb<sub>2</sub>O<sub>6</sub> composite prepared in this work demonstrates an outstanding degradation efficiency and expectable low cost.

## Electrochemical analysis

Electrochemical testing can effectively characterize the catalytic activity and band structure of photocatalytic materials [41]. Mott–Schottky (MS) tests were carried out to estimate the band structure of the catalysts. As shown in Fig. 12a, CuNb<sub>2</sub>O<sub>6</sub> is an N-type semiconductor with a flat band potential ( $V_{FB}$ ) of  $-1.53$  V (vs. Ag/AgCl). Considering that the value of  $V_{FB}$  of N-type semiconductors is usually about 0.1 V higher than the conduction band edge potential ( $E_{CB}$ ) and Ag/AgCl potential is 0.20 V [42], the CB edge potential of CuNb<sub>2</sub>O<sub>6</sub> was estimated to be  $-1.02$  V (vs. NHE, pH=7). Similarly, the CB edge potential of 11% Ag/g-C<sub>3</sub>N<sub>4</sub>/CuNb<sub>2</sub>O<sub>6</sub>-4 composite and g-C<sub>3</sub>N<sub>4</sub> was about  $-0.91$  and  $-0.83$  V, respectively (vs. NHE, pH=7).

Photocurrent measurement can characterize the photocatalytic activity of the catalyst. As shown in Fig. 12b, the photocurrent response of o-CNO was significantly lower than that of g-C<sub>3</sub>N<sub>4</sub> and 11% Ag/g-C<sub>3</sub>N<sub>4</sub>/CuNb<sub>2</sub>O<sub>6</sub>-4 composite. The photocurrent response of 11% Ag/g-C<sub>3</sub>N<sub>4</sub>/CuNb<sub>2</sub>O<sub>6</sub>-4 composite was slightly higher than that of g-C<sub>3</sub>N<sub>4</sub>, which could be attributed to the formation of g-C<sub>3</sub>N<sub>4</sub>/CuNb<sub>2</sub>O<sub>6</sub>-4 heterojunction.

The electrochemical impedance spectra (EIS) of the samples are shown in Fig. 12c. Compared with the other samples, 11% Ag/g-C<sub>3</sub>N<sub>4</sub>/CuNb<sub>2</sub>O<sub>6</sub>-4 composite demonstrates the smallest radius in the Nyquist diagram, suggesting the smallest electric resistance and the best charge transfer efficiency [43]. This indicates that Ag shows a charge transfer effect in the photocatalyst after the formation of composite semiconductor.

**Table 2** Comparison of degradation efficiency of dyes by different catalysts

Catalyst	Dosage (mg)	Dyes	Light source	Degrading time (min)	$\eta$ (%)	References
CdS/Au/g-C <sub>3</sub> N <sub>4</sub>	50	10 mg/L RhB	300 W Xe lamp	10	90	[45]
C <sub>coke</sub> /g-C <sub>3</sub> N <sub>4</sub>	125	50 mg/L MB	150 W Xe lamp	120	25	[46]
Bi/Bi <sub>2</sub> WO <sub>6</sub> /g-C <sub>3</sub> N <sub>4</sub>	125	50 mg/L MB	150 W Hg lamp	120	67	[46]
Ag/g-C <sub>3</sub> N <sub>4</sub>	10	10 mg/L RhB	500 W Xe lamp	100	98	[27]
g-C <sub>3</sub> N <sub>4</sub> /Ag/TiO <sub>2</sub>	30	13.5 mg/L MO	Xe lamp	720	94	[47]
g-C <sub>3</sub> N <sub>4</sub> /Bi <sub>5</sub> O <sub>7</sub> I	50	10 mg/L MO	500 W Xe lamp	270	98	[48]
Al <sub>2</sub> O <sub>3</sub> /g-C <sub>3</sub> N <sub>4</sub>	5	10 mg/L RhB	50 W LED lamp	80	89	[49]
Ag/CuNb <sub>2</sub> O <sub>6</sub> /CuFe <sub>2</sub> O <sub>4</sub>	50	10 mg/L MB	1 kW halogen lamp	120	96	[21]
Ag/g-C <sub>3</sub> N <sub>4</sub> /CuNb <sub>2</sub> O <sub>6</sub>	10	10 mg/L RhB	200 W Xe lamp	120	82	This work

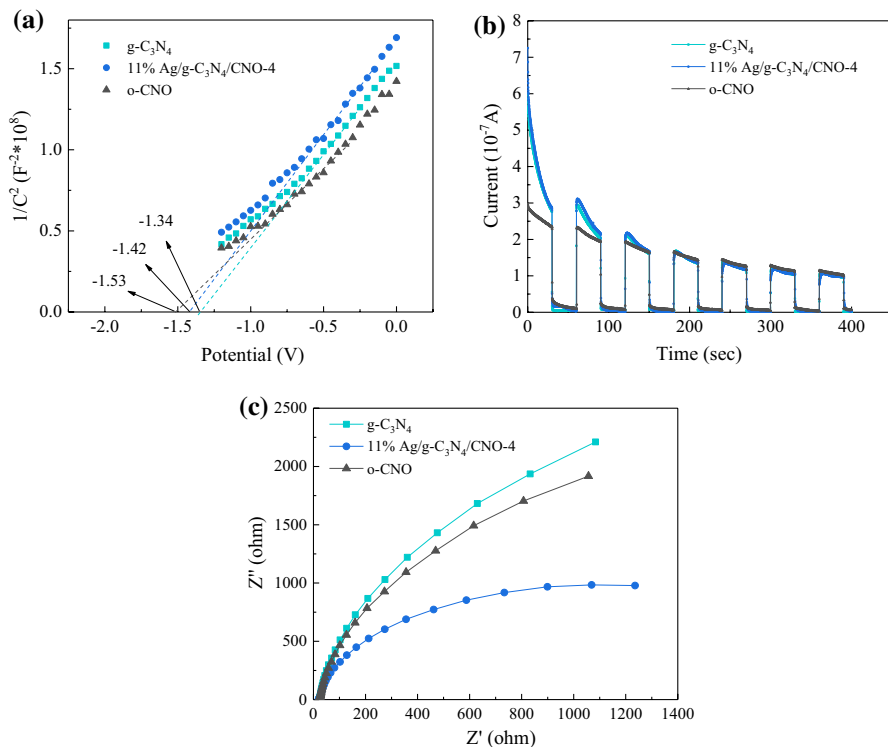


**Fig. 12** Electrochemistry test results of the as-synthesized photocatalysts

## Active species

To further study the photocatalytic mechanism of 11% Ag/g-C<sub>3</sub>N<sub>4</sub>/CNO-4 composite, free radical trapping experiments were carried out to determine the main active components involved in the photocatalytic process. The procedure was similar to the measurement of photocatalytic activity, except that the trapping agent was added in RhB dye solution. In the experiment, benzoquinone and isopropanol (IPA) were used as the traps for h<sup>+</sup>, ·O<sub>2</sub><sup>-</sup>, and ·OH radicals, respectively. The capture experiment results of 11% Ag/g-C<sub>3</sub>N<sub>4</sub>/CNO-4 composite for the degradation of RhB are shown in Fig. 13a. The degradation efficiency of 11% Ag/g-C<sub>3</sub>N<sub>4</sub>/CNO-4 on RhB inhibited significantly after the addition of oxalic acid, indicating that h<sup>+</sup> was the main reactive species in the photocatalytic process. In addition, the photocatalytic decolorization of RhB also inhibited after the addition of benzoquinone, indicating that ·O<sub>2</sub><sup>-</sup> radical also played a main role in the photocatalytic process. However, when IPA was added, the photocatalytic efficiency of the sample changed slightly. It indicates that ·OH plays a minor role in the photocatalytic process. In addition, according to the results of the ESR test shown in Fig. 13b–d, the presence of active free radicals, such as h<sup>+</sup>, ·O<sub>2</sub><sup>-</sup>, and

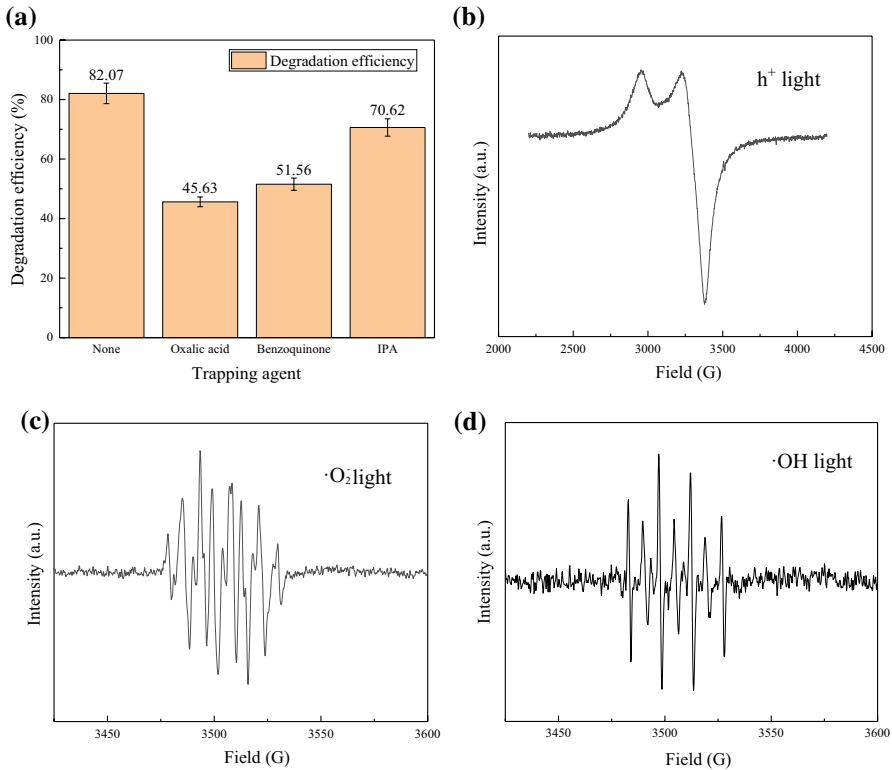


**Fig. 13** Results of **a** degradation efficiency of 11% Ag/g-C<sub>3</sub>N<sub>4</sub>/CNO-4 composite on RhB in free radical trapping experiments, **b** ESR assay of h<sup>+</sup>, **c** ·O<sub>2</sub><sup>-</sup>, and **d** ·OH

·OH, was confirmed [44]. As a result, the h<sup>+</sup> and ·O<sub>2</sub><sup>-</sup> were the main reactive radicals whereas the ·OH radical played an auxiliary role in the photocatalytic process for degradation of RhB.

### Degradation mechanism analysis

As the CB edge potentials of g-C<sub>3</sub>N<sub>4</sub>, 11% Ag/g-C<sub>3</sub>N<sub>4</sub>/CNO-4 composite, and o-CNO were -0.83, -0.91, and -1.02 V, respectively (vs. NHE, pH=7), the valence band (VB) edge potentials of g-C<sub>3</sub>N<sub>4</sub>, 11% Ag/g-C<sub>3</sub>N<sub>4</sub>/CNO-4 composite, and o-CNO can be easily calculated and were found to be +1.87, +1.40, and +0.88 V, respectively (Fig. 14).

It is known that there are two common routes for charge transfer between two different kinds of semiconductors. The first is the traditional type-II heterojunction and the second is the Z-scheme heterojunction. In the former case, electrons are transferred from the CB of the semiconductor with high CB edge potential to the CB of another semiconductor with low CB edge potential, and the holes move from the low potential VB to the high potential VB. However, in Z-scheme mechanism, the electrons in the

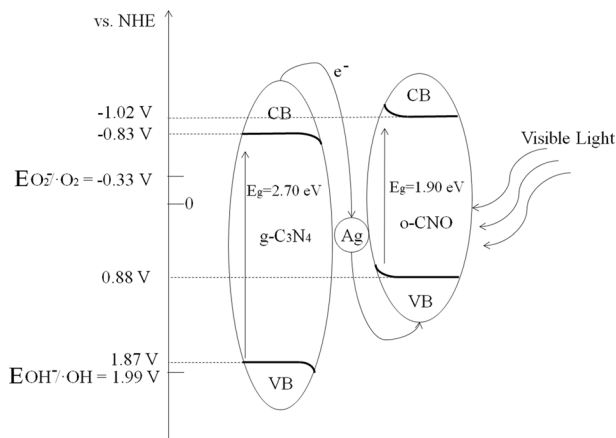


**Fig. 14** Photocatalytic mechanism sketch of Ag/g-C<sub>3</sub>N<sub>4</sub>/CNO composite for degradation of RhB

CB of a semiconductor directly recombine with the holes in the VB of the other semiconductor with a relatively lower oxidation potential. Therefore, the electrons and holes with high reduction and oxidation capacities are retained.

In the present work, according to the band structure of 11% Ag/g-C<sub>3</sub>N<sub>4</sub>/CNO-4 composite, ·OH radical was not produced during the photocatalytic process, because its VB edge potential was more negative than the potential of OH<sup>-</sup>/·OH electrode. However, the presence of ·OH radical was confirmed in the active species test and ESR test. Therefore, the hypothesis that the Ag/g-C<sub>3</sub>N<sub>4</sub>/CNO composite forms a traditional type-II heterojunction was inconsistent with the results of active species trapping and ESR experiments. We proposed a possible all-solid-state Z-scheme photocatalytic mechanism. Under visible light irradiation, g-C<sub>3</sub>N<sub>4</sub> and o-CNO can be excited to form electron-hole pairs and the photogenerated electrons can be transferred from VB to CB of g-C<sub>3</sub>N<sub>4</sub> phase. Subsequently, the Ag nanoparticles dispersed on the interface of g-C<sub>3</sub>N<sub>4</sub> and o-CNO act as a bridge for the transfer of electrons from CB of the g-C<sub>3</sub>N<sub>4</sub> phase to the VB of o-CNO phase, thereby inhibiting the recombination of photogenerated electrons and holes in individual semiconductors. Consequently, the electrons were excited to the CB of the CNO phase, and holes generated in the g-C<sub>3</sub>N<sub>4</sub> phase were completely spatially segregated, and therefore, the 11% Ag/g-C<sub>3</sub>N<sub>4</sub>/CNO composite provides a much stronger redox capacity and demonstrates better photocatalytic performance. Meanwhile, due to the formation of heterojunction, a built-in electric field was formed inside the catalyst, and the band edge of g-C<sub>3</sub>N<sub>4</sub> bends toward the side of higher oxidation potential, thus producing ·OH radical. Moreover, as a charge transfer channel, silver effectively retains the REDOX capability of all-solid-state Z-scheme heterojunction.

## Conclusion

In summary, an orthorhombic CuNb<sub>2</sub>O<sub>6</sub> phase was obtained in high purity via the calcination of hydrothermally synthesized CuNb<sub>2</sub>O<sub>6</sub> and Ag/g-C<sub>3</sub>N<sub>4</sub>/CuNb<sub>2</sub>O<sub>6</sub>-4 (mass ratio of g-C<sub>3</sub>N<sub>4</sub> to CuNb<sub>2</sub>O<sub>6</sub> was 1:4) composites with different Ag contents which were successfully prepared using the hydrothermal and photo-deposition method. The Ag content in Ag/g-C<sub>3</sub>N<sub>4</sub>/CuNb<sub>2</sub>O<sub>6</sub>-4 composites showed a significant effect on its photocatalytic efficiency and the 11% Ag/g-C<sub>3</sub>N<sub>4</sub>/CuNb<sub>2</sub>O<sub>6</sub>-4 composite showed the highest photocatalytic activity. An all-solid-state Z-scheme heterojunction was successfully fabricated by loading Ag onto the g-C<sub>3</sub>N<sub>4</sub>/CuNb<sub>2</sub>O<sub>6</sub> composite. The h<sup>+</sup> and ·O<sub>2</sub><sup>-</sup> were found to be the main active radicals in the photocatalytic degradation of RhB solution. Although the photocatalytic efficiency of Ag/g-C<sub>3</sub>N<sub>4</sub>/CuNb<sub>2</sub>O<sub>6</sub>-4 composites improved greatly as seen in the experiments, further study should be carried out to reduce the cost of photocatalysts in industrial applications.

**Acknowledgements** This work was supported by Zhejiang provincial key R&D program under Grant No. 2019C01088.

## Declarations

**Conflict of interest** No potential conflict of interest was reported by the authors.

## References

1. S. Lin, W. Liu, J. Environ. Eng. **120**, 2 (1994)
2. S.S. Lee, H. Bai, Z. Liu, D.D. Sun, Environ. Sci. Technol. **49**, 4 (2015)
3. V. Vaiano, O. Sacco, D. Sannino, P. Ciambelli, Appl. Catal. B Environ. **170–171**, 153 (2015)
4. A. Houas, H. Lachheb, M. Ksibi, E. Elaloui, C. Guillard, J.-M. Herrmann, Appl. Catal. B **31**, 2 (2001)
5. N. Al-Bastaki, Chem. Eng. Process. **43**, 12 (2004)
6. A.N. Soon, B.H. Hameed, Desalination **269**, 1 (2011)
7. G. Liu, M. Feng, M. Tayyab, J. Gong, M. Zhang, M. Yang, K. Lin, J. Hazard. Mater. **412**, 125224 (2021)
8. C. Rafols, D. Barcelo, J. Chromatogr. A **777**, 1 (1997)
9. I. Oller, S. Malato, J.A. Sánchez-Pérez, Sci. Total Environ. **409**, 20 (2011)
10. N. Fajrina, M. Tahir, Chem. Eng. J. **374**, 1076 (2019)
11. C. Namasivayam, D. Sangeetha, J. Hazard. Mater. **135**, 1 (2006)
12. V.K. Gupta, Suhas, J. Environ. Manag. **90**, 8 (2009)
13. E. Forgaes, T. Cserhádi, G. Oros, Environ. Int. **30**, 7 (2004)
14. L. Zhang, H.H. Mohamed, R. Dillert, D. Bahnemann, J. Photochem. Photobiol. C **13**, 4 (2012)
15. Y. Liu, Q. Zhu, M. Tayyab, L. Zhou, J. Lei, J. Zhang, Solar RRL **5**, 11 (2021)
16. Y.C. Zhang, B. Fu, Q. Liu, J. Alloys Compd. **477**, 1 (2009)
17. A. Kormányos, A. Thomas, M.N. Huda, P. Sarker, J.P. Liu, N. Poudyal, C. Janáky, K. Rajeshwar, J. Phys. Chem. C **120**, 29 (2016)
18. X. Ye, Z. Wen, R. Zhang, H. Ling, J. Xia, X. Lu, J. Power Sources **483**, 22919 (2021)
19. M.G.B. Drew, R.J. Hobson, V.T. Padayatchy, J. Mater. Chem. **3**, 8 (1993)
20. S. Kamimura, S. Abe, T. Tsubota, T. Ohno, J. Photochem. Photobiol. A Chem. **356**, 263 (2018)
21. Y. Tang, D. Zhang, Y. Li, B. Huang, H. Li, X. Pu, Y. Geng, Sep. Purif. Technol. **220**, 78 (2019)
22. Y. Kang, Y. Yang, L.-C. Yin, X. Kang, G. Liu, H.-M. Cheng, Adv. Mater. **27**, 31 (2015)
23. W.-J. Ong, L.-L. Tan, Y.H. Ng, S.-T. Yong, S.-P. Chai, Chem. Rev. **116**, 12 (2016)

24. J. Fu, J. Yu, C. Jiang, B. Cheng, *Adv. Energy Mater.* **8**, 3 (2018)
25. L. Guan, N. Xu, X. Liu, Y. Zhao, H. Li, J. Sun, J. Wu, Z. Ying, *Carbon* **79**, 578 (2014)
26. Y. Chen, X. Bai, *Catalysts* **10**, 1 (2020)
27. K. Qi, Y. Li, Y. Xie, S.-Y. Liu, K. Zheng, Z. Chen, R. Wang, *Front. Chem.* **7**, 91 (2019)
28. Y. Fu, T. Huang, L. Zhang, J. Zhu, X. Wang, *Nanoscale* **7**, 32 (2015)
29. X. Zhou, Z. Luo, P. Tao, B. Jin, Z. Wu, Y. Huang, *Mater. Chem. Phys.* **143**, 3 (2014)
30. M. Faisal, A.A. Ismail, F.A. Harraz, S.A. Al-Sayari, A.M. El-Toni, M.S. Al-Assiri, *Mater. Des.* **98**, 223 (2016)
31. S. Ma, S. Zhan, Y. Jia, Q. Shi, Q. Zhou, *Appl. Catal. B Environ.* **186**, 77 (2016)
32. L. Ge, C. Han, J. Liu, Y. Li, *Appl. Catal. A Gen.* **409–410**, 215 (2011)
33. M. Arfan, I. Hussain, Z. Ahmad, A. Afzal, T. Shahid, A.G. Wattoo, M. Rafi, A. Zeb, M.I. Shahzad, S. Zhenlun, *Cryst. Res. Technol.* **57**, 2100230 (2022)
34. X.-C. Zheng, S.-P. Wang, S.-R. Wang, S.-M. Zhang, W.-P. Huang, S.-H. Wu, *Mater. Sci. Eng. C* **25**, 4 (2005)
35. M.T. Qamar, M. Aslam, I.M.I. Ismail, N. Salah, A. Hameed, *ACS Appl. Mater. Interfaces* **7**, 16 (2015)
36. P. Steiner, H. Höchst, *Zeitschrift für Phys. B Condens. Matter* **35**, 1 (1979)
37. Y. Wang, L. Zhang, R. Cao, Q. Miao, J. Qiu, *Appl. Phys. A* **115**, 4 (2014)
38. M. Grobelny, M. Kalisz, M. Mazur, D. Wojcieszak, D. Kaczmarek, J. Domaradzki, M. Świniarski, P. Mazur, *Thin Solid Films* **616**, 64 (2016)
39. Y. Shi, S. Jiang, K. Zhou, B. Wang, B. Wang, Z. Gui, Y. Hu, R.K.K. Yuen, *RSC Adv.* **4**, 6 (2014)
40. N.K.R. Bogireddy, S. Godavarthi, M.K. Kesarla, V. Agarwal, L. Martínez-Gómez, *J. Environ. Chem. Eng.* **8**, 6 (2020)
41. M. Tayyab, Y. Liu, S. Min, R. Muhammad-Irfan, Q. Zhu, L. Zhou, J. Lei, J. Zhang, *Chin. J. Catal.* **43**, 4 (2022)
42. W. Zhang, P. Xing, J. Zhang, L. Chen, J. Yang, X. Hu, L. Zhao, Y. Wu, Y. He, *J. Colloid Interface Sci.* **590**, 548 (2021)
43. H. Liang, T. Li, J. Zhang, D. Zhou, C. Hu, X. An, R. Liu, H. Liu, *J. Colloid Interface Sci.* **558**, 85 (2020)
44. D. Dvoranová, V. Brezová, M. Mazúr, M.A. Malati, *Appl. Catal. B* **37**, 2 (2002)
45. D. Peng, H. Wang, K. Yu, Y. Chang, X. Ma, S. Dong, *RSC Adv.* **6**, 81 (2016)
46. M. Sierra, E. Borges, P. Esparza, J. Méndez-Ramos, J. Martín-Gil, P. Martín-Ramos, *Sci. Technol. Adv. Mater.* **17**, 1 (2016)
47. Y. Chen, W. Huang, D. He, Y. Situ, H. Huang, *ACS Appl. Mater. Interfaces* **6**, 16 (2014)
48. H. Huang, C. Liu, H. Ou, T. Ma, Y. Zhang, *Appl. Surf. Sci.* **470**, 205 (2019)
49. Y. Zheng, C. Wei, Q. An, J. Yu, S. Xu, L. Li, *New J. Chem.* **45**, 36 (2021)

**Publisher's Note** Springer Nature remains neutral with regard to jurisdictional claims in published maps and institutional affiliations.

Springer Nature or its licensor holds exclusive rights to this article under a publishing agreement with the author(s) or other rightsholder(s); author self-archiving of the accepted manuscript version of this article is solely governed by the terms of such publishing agreement and applicable law.